CO$_2$ Storage and Flow Capacity Measurements on Idealized Shales from Dynamic Breakthrough Experiments

Hamza Aljamaan,[†] Randall Holmes,[‡] Vikram Vishal,[§] Reza Haghpanah,[∥] Jennifer Wilcox,[⊥] and Anthony R. Kovscek*,[†]

[†]Department of Energy Resources Engineering, Stanford University, Stanford, California 94305-2220, United States
[‡]Department of Earth System Science, Stanford University, Stanford, California 94305-2220, United States
[§]Department of Earth Sciences, Indian Institute of Technology Bombay, Powai, Mumbai, 400076, India
[∥]Dow Corning Corporation, Midland, Michigan 48686, United States
[⊥]Chemical and Biological Engineering Department, Colorado School of Mines, Golden, Colorado 80401, United States

ABSTRACT: Dynamic column breakthrough (DCB) measurements were carried out on idealized shale samples for the first time, based on a custom-designed system. To better understand the contribution of different shale minerals on flow and storativity, measurements were carried out on composition-controlled shales having known weight percentages of total organic carbon (TOC) and illite. CO$_2$ was assessed for its potential for sequestration, as well as its applicability as a fracturing fluid for enhanced gas recovery in shale formations. Experimental results reveal an increase in permeability and CO$_2$ adsorption with either increasing TOC or illite content. This is attributed to the complex porous structure of kerogen, as well as the interlayering characteristics of clay minerals, resulting in large surface area and pore volume ratios. Permeant permeability reduction was noted with CO$_2$ due to adsorption-induced swelling that is proportional to the amount of gas adsorbed. Helium permeability post CO$_2$ adsorption decreased by 63% and 31.5% for the 46.3% and 25.4% illite series, respectively. In fact, DCB experiments reveal the potential for CO$_2$ storage in shale formations with adsorption capacities exceeding that of CH$_4$ by 4−12 times, depending on the content of TOC and illite. Through a series of low-pressure gas adsorption experiments, it was found that each weight percent increase in TOC has a larger influence on the pore volume and surface area, compared to each weight percent increase in illite content. An ~3.5 wt % increase in TOC leads to an ~0.005 cm^3/g increase in pore volume, whereas it takes a ~20 wt % increase in illite to achieve a 0.003 cm^3/g increase. The TOC series pore volume increases by ~1.4 × 10^{-3} cm^3/g for each weight percent increase in TOC, whereas the illite series pore volume only increases by ~0.4 × 10^{-3} cm^3/g for each weight percent increase in illite content. The coupled results clearly establish the comparative role of the organic versus inorganic adsorbing components of gas shales while overcoming the material heterogeneity through the investigation of "idealized" compositions.

1. INTRODUCTION

Porosity, permeability, tensile strength, and compressive strength are among the main attributes of a reservoir to establish its long-term utility for recovery of the hydrocarbon present in it.[1−5] Challenges in gas shales include extremely low matrix permeability (ranging from micro to nano Darcy), very fine grain sizes, storage of gas in both organic and inorganic components, and the structural integrity of the rock itself. The presence of extremely large surface area in the micropores and mesopores, however, enables large volumes of gases to be stored in shales by adsorption.[6] Further, the pores in shales are extremely heterogeneous, in terms of their shapes, sizes, and structures. Hence, different gases access pores differently.[7] Several approaches have been attempted to experimentally and mathematically model these heterogeneities and to establish a more accurate relationship among gas adsorption and pore characteristics in shales.[8−10] Efforts have been made to achieve most reasonable estimates for gas storage in shales and it is found that the same is dependent on several factors, such as thermal maturity, formation temperature, moisture content, and pore characteristics.[11−20] One of the important factors is the proportion of organic and inorganic constituents in the shale and their intraparticle pore structure.[7,18] Shales are often rich in

organic matter and clays of different types making up a large portion of the rock system. Therefore, it is important to investigate the role of mineral and organic matter composition of shale plays on gas storage and transport capacities.

It has been established that pores in the organic and the inorganic content of shale are the spaces for gas storage, while the natural and hydraulic fractures enable transport of fluids through these pores.[7,21,22] High-pressure CO$_2$ phases are among the proposed supplements for fracturing fluids. They additionally help in the recovery of natural gas by preferential adsorption of CO$_2$ to the pore surfaces.[23−27] Adsorption not only enables large volumes of CO$_2$ to be stored after the strata fracturing is complete, but may also enhance the recovery of CH$_4$ from shale plays.

Recent years have witnessed the application of various techniques for estimating the gas storage capacity of shales at various pressure and temperature conditions. These include high-pressure mercury injection,[28] scanning electron microscopy,[29−32] computed tomography,[33,34] small-angle neutron

scattering,[6,35] and low-pressure gas adsorption.[15,36,37] With its own set of strengths and weaknesses for each technique, these are only capable of giving an estimate of one or more of the following: porosity, pore volume, and pore-size distribution. These methods are not capable of describing the kinetics of gas adsorption through reservoir rocks. Therefore, in this work, we introduce the concept of dynamic column breakthrough as applied to gas shales. Dynamic breakthrough allows both gas storage capacity and permeability of the shale to be estimated.

Gas adsorption capacities of shales have been measured for samples from various basins; however, the samples have been examined on an equilibrium basis only. The static techniques, such as gravimetric and volumetric methods, are commonly used for estimating the storage potential of gas shales. As the operation of either CH_4 desorption (in the case of gas shale extraction) or CO_2 adsorption (as in the case of carbon sequestration) are dynamic and controlled by the changes in pressure conditions, it is anticipated that using a dynamic test rig provides a better understanding of the gas-shale adsorption equilibrium processes. Such experiments provide kinetic information, help to estimate the performance of the rock column, and enable the calibration of process models that may be scaled up.[38] Dynamic column breakthrough (DCB) studies have previously been carried out for investigating gas adsorption in zeolites,[39] silica gel,[40] tree leaf powder,[41] copper trimesate metal,[42] nitrogen-doped porous carbon,[43] and graphitic carbon.[44] Similar experiments, however, have not been conducted for gas shale investigation.

The design of dynamic experiments for understanding the kinetics of adsorbate−adsorbent interaction can be ascertained by several techniques summarized by Sircar.[45] The advantage of a DCB setup is that the exiting phase composition is measured instantaneously using a mass spectrometer. The gas effluent indicates not only the time of breakthrough but also the compositional changes after crossing through the adsorbent. This characterizes the amount of gas adsorbed in the fine pores of the adsorbent. Importantly, results can be scaled up to estimate the gas storage capacity. The pressure differential developed at the two ends of the rock column enables measurement of the apparent permeability of the shale using Darcy's law.

Because the composition of the adsorbent varies, a change in the breakthrough characteristics of the selected adsorbate is expected. Initial experiments were conducted on two Utica crushed samples to assess the impact of mineralogy on CO_2 adsorption in shales but were not conclusive. The samples were obtained from two different depths, as shown in Table 1. X-ray diffraction (XRD) data from the nearest depth was used to represent the mineralogy of these two samples. Figure 1 shows the breakthrough profile for both samples with insignificant difference in the delay time. At 23.8 °C and a CO_2 partial

pressure of 279.5 psi, the adsorption capacity was 130.4 and 121.5 scf (standard cubic feet)/ton for U1 and U2, respectively. This could be attributed to the heterogeneous nature of shale formations.[46,47] The ternary diagram shown in Figure 2 illustrates the variation in shale components at distances of <1 ft in the reservoir for both Haynesville and Utica shale plays. Relating samples to nearby XRD data could be misleading and hence, consistent properties of TOC and clay are required for an accurate assessment. This finding motivated the use of controlled compositions of idealized shale to estimate the adsorption kinetics for CO_2 in this paper.

2. SAMPLE DESCRIPTION

To obtain consistent properties of TOC and clay in the DCB experiments, idealized shales were created to control the various challenges associated with the heterogeneous nature of shales. The idealized shales were created with varying compositions based on the weight percent of three main components common to many shales: (1) TOC, represented by the naturally occurring kerogen of a Marcellus shale; (2) Green River Formation illite (Ward's Natural Science Establishment, Rochester, NY), to represent clay; and (3) powdered SiO_2 (Sigma−Aldrich, 99.5% SiO_2, 325 mesh powder) to represent quartz. The samples were initially meshed from 250 μm to 45 μm. Then, 20.0 g of idealized samples were created at the desired relative weight percentage of each component in each of the idealized sample series. Pyrite also exists naturally in the shale and the illite, and was included in the weight percent calculations. In this manner, we have an accurate representation of shale mineralogy on which to study the impact upon storage and flow capacity. Details for each shale component follow.

2.1. Total Organic Carbon (TOC). The TOC of the Marcellus shale was measured by placing ∼2.00 mg of the powdered shale sample into silver receptacles, removing all inorganic carbon by successive treatment with 40 mL HCl (1N) acid digestion, followed by up to 4 h of drying at 60 °C. Removal of inorganic carbon was confirmed by observing the sample under a microscope until no effervescence was observed with application of additional acid. The samples were dried at 40 °C for at least 96 h before flash combustion in pure oxygen on a Carlo Erba NA 1500 Series 2 elemental analyzer. The gases in the Carlo Erba elemental analyzer are passed over a combustion catalyst of chromium trioxide, then a reduction reactor of metallic copper kept at 650 °C, as well as through a water removal stage using magnesium perchlorate. A stream of 4.8 grade helium (99.998% pure) carries the remaining carbon and nitrogen (C/N) gases past a chromatographic column, which separates them for the final stage. The thermal conductivity detector in the final stage generates an electrical signal in direct proportion to the C/N concentrations as the gases flowing by the column. The C/N concentrations of the samples are determined by comparing them to the signatures of a laboratory-grade standard of known carbon/nitrogen concentrations, such as acetanilide, which were used to create a calibration curve, and were also combusted between at least every 12th sample to adjust for any drift. A linear calibration curve of at least five standards were fit with a correlation coefficient of $r^2 \approx 0.9999$. The Marcellus shale TOC of 12.5% was used to calculate the TOC weight percentage needed for each idealized shale admixture. A negligible amount of TOC was assumed to be present in the Green River Shale illite, so it was not analyzed for TOC.

Table 1. Utica Powdered Samples and X-ray Diffraction (XRD) Data from a Nearby Depth

sample	depth (ft)
U1 (H)	6281.2
U2 (H)	6529

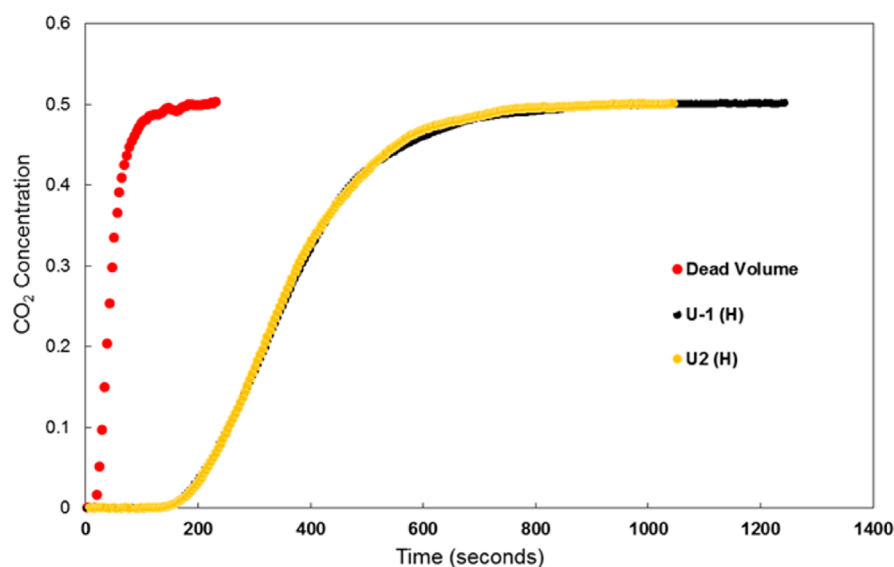|	Totals		
top−bottom (ft)	total organic content, TOC (%)	clays	carbs.	other
6282.85−6383.15	2.368	49	12	39
6527.85−6528.15	2.151	11	80	9

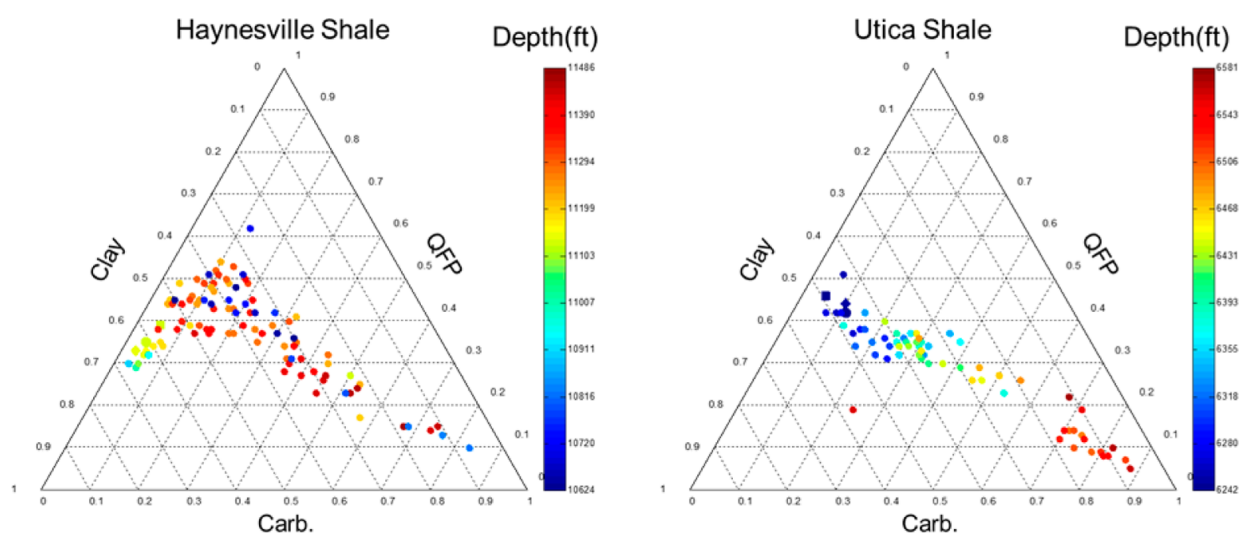**Figure 1.** CO_2 breakthrough on Utica powdered samples U1 and U2.

Figure 2. Haynesville and Utica mineralogy at varying depths.[48]

2.2. X-ray Diffraction (XRD). The composition of the Marcellus shale and Green River Shale illite were obtained through X-ray diffraction (XRD). The compositions of the illite and Marcellus shale were determined by collecting X-ray diffractograms on a Rigaku model CM2029 powder X-ray diffractometer. A Cu Kα X-ray source was used to create diffractograms that were determined over the 2θ range of $5°-70°$. The JADE diffraction software was used to analyze the data.[49] The four most intense diffraction peaks were used to match given mineral phases with peak identifications, in accordance with the National Institute of Standards and Technology (NIST) database. The Marcellus shale XRD results of 3.3% pyrite, 36.8% quartz, and 47.3% illite were used to calculate the relative weights of Marcellus shale needed in each of the idealized sample series. Similarly, the Green River Shale illite XRD results of 3.8% pyrite, 42.1% quartz, and 54.1% illite, were used to calculate the relative weight of Illite needed in each of the idealized samples.

2.3. Idealized Shale Calculations. The relative weight percentages required for each of the components of each sample was predetermined as follows. First, an amount of Marcellus shale was weighed and the relative weight percentage of TOC that would be in a 20.0 g sample was calculated. Second, the relative weight percentage of powdered Green River illite was added and mixed into the Marcellus shale. The amount of pyrite and illite in the shale were calculated and the relative weight percentages were adjusted accordingly. The relative weight of quartz needed was calculated by subtracting the cumulative weight of both Marcellus shale and Green River Shale illite from 20.0 g to complete the relative sample weights. Lastly, the calculated amount of powdered crystalline quartz was added until each sample mass reached 20.0 g.

2.4. Total Organic Content (TOC) Series. The amount of Marcellus sample required to make 20.0 g of idealized samples with 2.0%, 5.5%, and 9.0% TOC (by mass) was 3.20, 8.80, and 14.4 g, respectively. The final 12.5% TOC sample was 20.0 g of natural Marcellus shale without any other components added. The amount of Green River Shale illite required to keep each TOC series sample at ~47.4% (by weight) was 1.52, 4.17, 6.83, and 9.48 g for each of the TOC series from smallest to largest TOC, respectively. The difference between the 20.0 g final
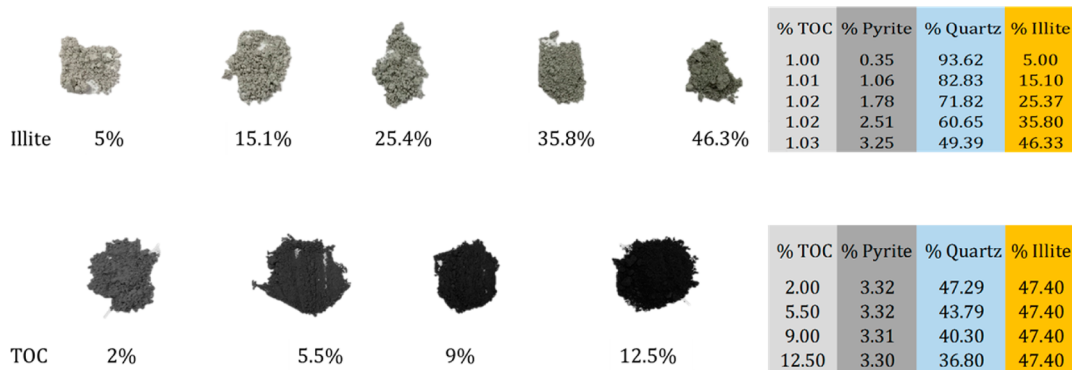
% TOC	% Pyrite	% Quartz	% Illite
1.00	0.35	93.62	5.00
1.01	1.06	82.83	15.10
1.02	1.78	71.82	25.37
1.02	2.51	60.65	35.80
1.03	3.25	49.39	46.33

% TOC	% Pyrite	% Quartz	% Illite
2.00	3.32	47.29	47.40
5.50	3.32	43.79	47.40
9.00	3.31	40.30	47.40
12.50	3.30	36.80	47.40

Figure 3. Idealized shale samples for TOC and illite content series.
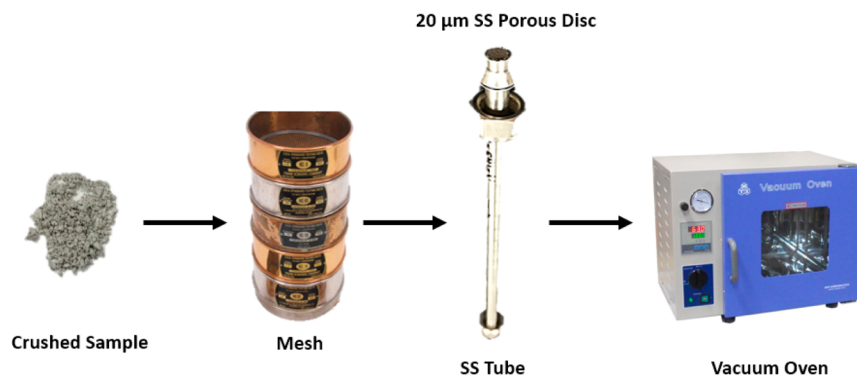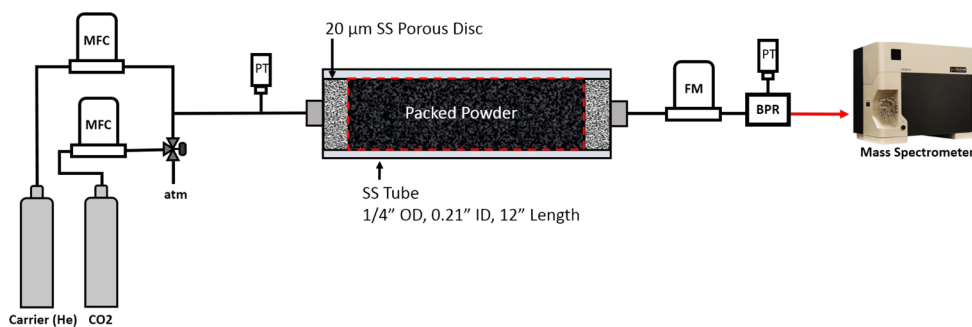

Figure 4. Idealized shale sample preparation.

Figure 5. Experimental schematic for dynamic breakthrough apparatus.

sample weight and the mixtures of TOC and illite was determined by adding SiO_2.

2.5. Illite Series. The illite series all had 1.0% TOC by mass and incrementally varying amounts of illite. The amount of Marcellus sample required to make 20.0 g of each of the idealized illite samples with 1.0% TOC, was 1.6 g each. The illite series required 0.44, 4.14, 7.84, 11.54, and 15.23 g of Green River Shale illite to create samples with 5.0%, 15.10%, 25.4%, 35.8% and 46.3% illite. The difference between the 20.0 g final sample weight and the Marcellus and Green River Shale illite components was determined by adding SiO_2. While the 35.8% (by weight) illite sample was also prepared, it was apparent from the difference in pore volumes and surface areas of the 5%, 25.4%, 15.1%, and 46.3% illites, that finer resolution would not add appreciable benefit to the analysis. As such, the 35.8% sample was prepared, but it was not run for analysis.

2.6. Sample Preparation. The powder was then packed into a 1-ft-long stainless steel (SS) tube with an outer diameter of 0.25 in. and a wall thickness of 0.02 in. The SS tube was sealed with a 20 μm supersmall-particle-filtering stainless steel porous disc from both ends. This ensured the entrapment of powder within the packed tube. The maximum pressure rating of the packed SS tube was 3500 psi at 22.2 °C. Each tube contained 7 g of each sample measured by a Mettler Toledo ME-TE analytical balance with an accuracy of ±0.2 mg. The sample was then dried and outgassed at 70 °C, as shown in Figures 3 and 4.

3. METHODOLOGY

3.1. Dynamic Column Breakthrough Experiment. The experimental setup was custom-built to estimate gas sorption based on the dynamic breakthrough technique. The physics of this experiment revolve around injecting a gas mixture of known composition at a constant pressure and flow rate from an upstream reservoir across a test sample and a downstream reservoir. The outlet is connected directly to a mass spectrometer to analyze the mixture concentration to ensure
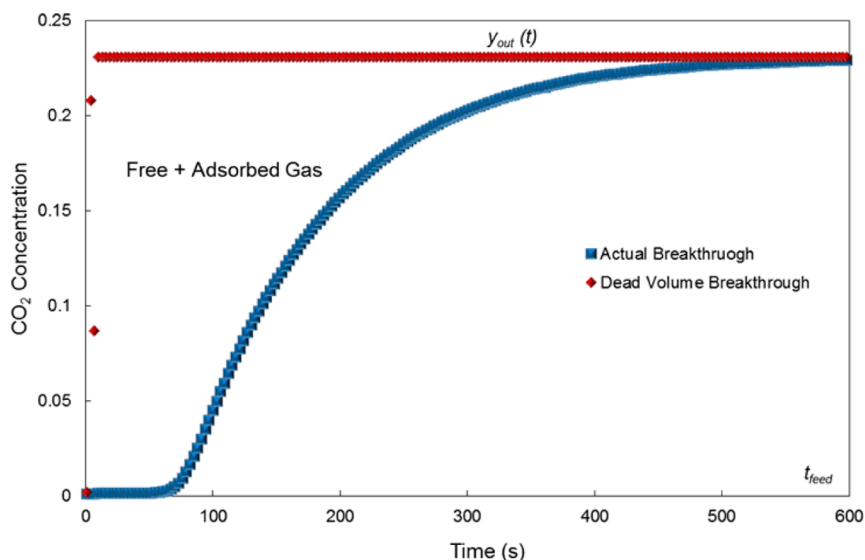
Figure 6. Dynamic breakthrough void versus actual concentration signal illustration.

sorbent breakthrough is complete. This is indicated when the exit sorbent concentration increases to reach the feed level.

The experimental setup, as shown in Figure 5, consists of the following: He and CO_2 gas cylinders with a purity of 99.999% and 99.998%, respectively, packed column, upstream and downstream strain gauge pressure transducers (PT) (type Super TJE and Precise Sensors, Inc.), Extrel Max300-LG mass spectrometer, Brooks SLA5850 digital mass flow controllers (MFCs), Brooks SLA5860 digital mass flow meter (MFM), and SS high back-pressure regulator (BPR). The MFC is used to regulate the flow rate of each injected gas across the core holder. The MFM is located at the exit of the core holder to measure the flow rate at the outlet with time. The accuracy of the MFC and MFM is ±1.0% for flow rates ranging 20% to 100% of full scale (200 cm^3/min) and ±0.2% of full scale for rates below 20% of full scale. Both transducers have an accuracy of 0.05% of full scale (1000 psi) and an additional temperature error of <0.0015% of full scale per °F. The BPR is used to control the pressure across the system. The mass spectrometer is used to measure the effluent gas concentration every second.

The sequence of this experiment is as follows.

- Saturate the system with a pure carrier gas (helium) at a known flow rate, pressure, and temperature.
- Ensure the system is fully flushed by monitoring the composition of the gas at the outlet.
- At $t = 0$, introduce a change in the gas mixture while maintaining the same total flow rate by using the mass flow controllers.
- Monitor the response from the mass spectrometer until sorbent breakthrough is achieved, as shown in Figure 6.

We determine the amount adsorbed from the breakthrough experiment by a simple mass balance that is defined as

$$\text{accumulation} = (\text{number of moles in})$$
$$- (\text{number of moles out}) + \text{generation}$$
$$- \text{consumption} \tag{1}$$

The accumulation is computed by subtracting the moles going into the column from the moles exiting the column.

There is neither generation nor consumption in the current experiment. The number of moles in is computed as follows:

$$\text{number of moles in} = Q_{in} \times \frac{P_{sc}T}{T_{sc}P} \times y_{feed} \times \frac{P}{RT} \times t_{feed} \tag{2}$$

where Q_{in} (given in scm/min) is the inlet volumetric flow rate, P the pressure (bar), T the temperature (K), R the gas compressibility factor (m^3 bar K^{-1} mol^{-1}), t_{feed} the duration of the feed (min), and y_{feed} the concentration of the feed.

The number of moles out is calculated as

$$\text{number of moles out} = \int_0^{t_{feed}} Q_{out}(t) \times \frac{P_{sc}T}{T_{sc}P} \times y_{out}(t) \times \frac{P}{RT} \, dt \tag{3}$$

where $Q_{out}(t)$ is the outlet volumetric flow rate, as a function of time; P is the pressure; T is the temperature; R is the gas compressibility factor; and $y_{out}(t)$ is the concentration of the feed at the outlet, as a function of time.

The accumulation term is the summation of the gas in the bulk and solid phase and is defined as

$$\text{accumulation} = \phi \times A \times L \times \frac{\sum_{i=1}^{N_c} y_i P}{RT} + q^* \tag{4}$$

where ϕ is the porosity of the sample, A the cross-sectional area (m^2), L the length of the sample (m), P the pressure, y_i the gas concentration of component i, T the temperature, R is the gas compressibility factor, and q^* the equilibrium loading (moles). Equation 4 is rearranged to solve for q^*. The propagation of error represented by error bars is primarily associated with the uncertainty of flow rate, pressure, and pore volume measurement, and this error is calculated as follows:

$$\delta q^* = \sqrt{\left[\sum_{i=1}^{2} \left(\frac{\partial q^*}{\partial P_i} \delta P_i \right)^2 + \left(\frac{\partial q^*}{\partial \phi} \delta \phi \right)^2 + \sum_{i=1}^{N_c} \left(\frac{\partial q^*}{\partial Q} \delta Q \right)^2 \right]} \tag{7}$$

The complex interplay between flow and storage capacity is essential for understanding the applicability of carbon storage at the field scale. The design of the breakthrough setup allows for simultaneous measurements of permeability and adsorption. Permeability measurements at the powder scale allows us to

determine the impact of mineralogy on flow capacities. Using the Scheidegger[50] equation, which incorporates gas compressibility, we estimate the permeability (k) as follows:

$$k = \frac{2Q\mu L P_{\text{down}}}{A(P_{\text{up}}^2 - P_{\text{down}}^2)} \tag{8}$$

where k is the permeability (m^2), Q the flow rate (cm^3/min), μ the gas viscosity (Pa s) (based on the multiparameter correlation technique for calculating gas mixture viscosities),[51] L the sample length (m), P_{down} the downstream pressure (Pa), P_{up} the upstream pressure (Pa), and A is the cross-sectional area (m^2). The error bar associated with permeability is a function of both the uncertainty in the flow rate and pressure transducer reading and is calculated as

$$\delta k = \sqrt{\left[\sum_{i=1}^{2} \left(\frac{\partial k}{\partial P_i} \delta P_i \right)^2 + \sum_{i=1}^{N_c} \left(\frac{\partial q^*}{\partial Q} \delta Q \right)^2 \right]} \tag{9}$$

3.2. Volumetric Pore Volume Experiment. In order to determine the free gas occupying the packed bed and, hence, quantify the adsorbed phase, a volumetric apparatus was also custom-designed. Helium was used as a probe gas. Several reasons make helium an ideal gas to perform such experiments. It provides a good means for accessing micropores, because of its small molecular size (0.26 nm). It is also an inert gas that is close to ideal and, hence, insignificant adsorption is likely to occur. The experimental schematic is shown in Figure 7 and
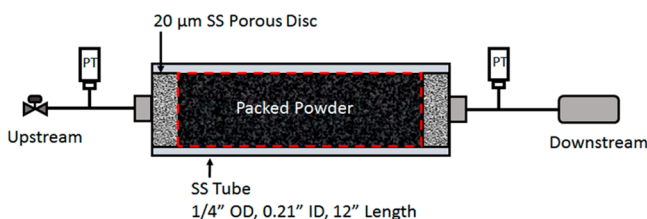

Figure 7. Volumetric porosity experimental schematic.

consists of two pressure transducers (PTs), an upstream and downstream volume, and a packed column. The dead volume of the system is measured with a water pressure pump (Teledyne Isco Syringe type, Model 500D) with an accuracy of ± 0.01 cm^3. The upstream volume is initially charged with helium at a certain pressure. The valve separating both volumes is opened, and the gas is allowed to expand into the sample and downstream volume. The pressure pulse is monitored with time until equilibrium is reached.

Using Boyle's law, we estimate the effective porosity of the sample as

$$\phi = \frac{\frac{P_1 V_1 / Z_1 - P_3 V_1 / Z_3}{P_3 / Z_3 - P_2 / Z_2} - V_2}{V_{\text{bulk}}} \tag{10}$$

where P_1 is the reference pressure in the upstream volume (psia), V_1 the upstream volume (cm^3), P_2 the reference pressure in the downstream volume (psia), V_2 (cm^3) the downstream volume, and V_{bulk} is the sample bulk volume (cm^3). P_3 is the final equilibrium pressure (psia) and Z_1, Z_2, and Z_3 are the compressibility factors for each specific pressure. We assume $Z = 1$ when using He, because of its ideality over the pressures and temperatures employed in the experiment. The uncertainty in porosity, represented by error bars, is estimated

based on the variable uncertainty of the dead volumes and pressure transducer fluctuations and is estimated as follows:

$$\delta \Phi = \sqrt{\left[\sum_{i=1}^{3} \left(\frac{\partial \Phi}{\partial P_i} \delta P_i \right)^2 + \sum_{i=1}^{2} \left(\frac{\partial \Phi}{\partial V_i} \delta V_i \right)^2 + \left(\frac{\partial \Phi}{\partial V_{\text{bulk}}} \delta V_{\text{bulk}} \right)^2 \right]} \tag{11}$$

3.3. Low-Pressure Gas Adsorption. Low-pressure gas adsorption isotherms were measured using an Autosorb iQ$_2$ instrument (Quantachrome Instruments). The samples were outgassed at a pressure of 10^{-3} bar for 18 h at 60 °C. Fine-mesopore (2.0−27.0427 nm) and larger-micropore (1.0297−2 nm) volumes were measured, with argon (99.999%) as a probe gas, at −186.15 °C, with the temperature held constant by a liquid argon bath. The resulting adsorption branch isotherms were used as an input parameter in the quenched solid density functional theory (QSDFT) model, assuming a carbon adsorbent and cylindrical pores. The QSDFT calculations were based on a 55-point adsorption branch with measurements made at relative pressures (P/P_0) spanning from 1.0 × 10^{-7} to 0.995. Each point was required to maintain an equilibration time of at least 5 min. The QSDFT model truncates at a pore diameter of 27.0427 nm, and that does not include the entire span of relative pressures from the adsorption branch isotherm. The same samples were then outgassed again at a pressure of 10^{-3} bar for up to 18 h at 60 °C. Micropore volumes (pore widths of 0.3053−1.4748 nm) were measured using CO$_2$ (99.999%) as a probe gas at −0.15 °C, with the temperature held constant using a Julabo cooler bath. The resulting adsorption branch isotherms from the CO$_2$ measurements were used as an input parameter for the nonlocal density functional theory (NLDFT) model that assumes a carbon adsorbent having slit pores. The cumulative pore volume for each sample was fitted by using the smallest diameter pore from the argon analysis, where it conveniently overlapped with the CO$_2$ pore width.

4. RESULTS AND DISCUSSION

4.1. Dynamic Column Breakthrough Analysis. Dynamic column breakthrough experiments were carried out on several shale samples. Initially, the system was flushed with helium at a constant flow rate of 50 sccm (standard cubic centimeters per minute). The concentration of helium was monitored with time using the mass spectrometer to ensure that the system was completely flushed. Using the back-pressure regulator, the average pressure of the system was increased incrementally. At t = 0, a change in the feed concentration was introduced. The dead volume of the system was also measured in order to determine the moles in the free and adsorbed phases.

4.1.1. Total Organic Content (TOC) Analysis. Because of the significant variation in shale mineralogy, we utilize the concept of idealized shales as introduced earlier. We start with a sample of known components and then add pure illite and silica to vary the original composition. This way, we have an accurate representation of the impact of each added mineral on storage and flow capacity. We first tested samples with a TOC range of 2%−12.5%, similar to the wide range observed in many shale formations.[46] The effective porosity of each packed sample is determined from the volumetric apparatus. The results are shown in Figure 8, with the upstream and downstream pressure profiles as well as the resulting porosity evolution with time.
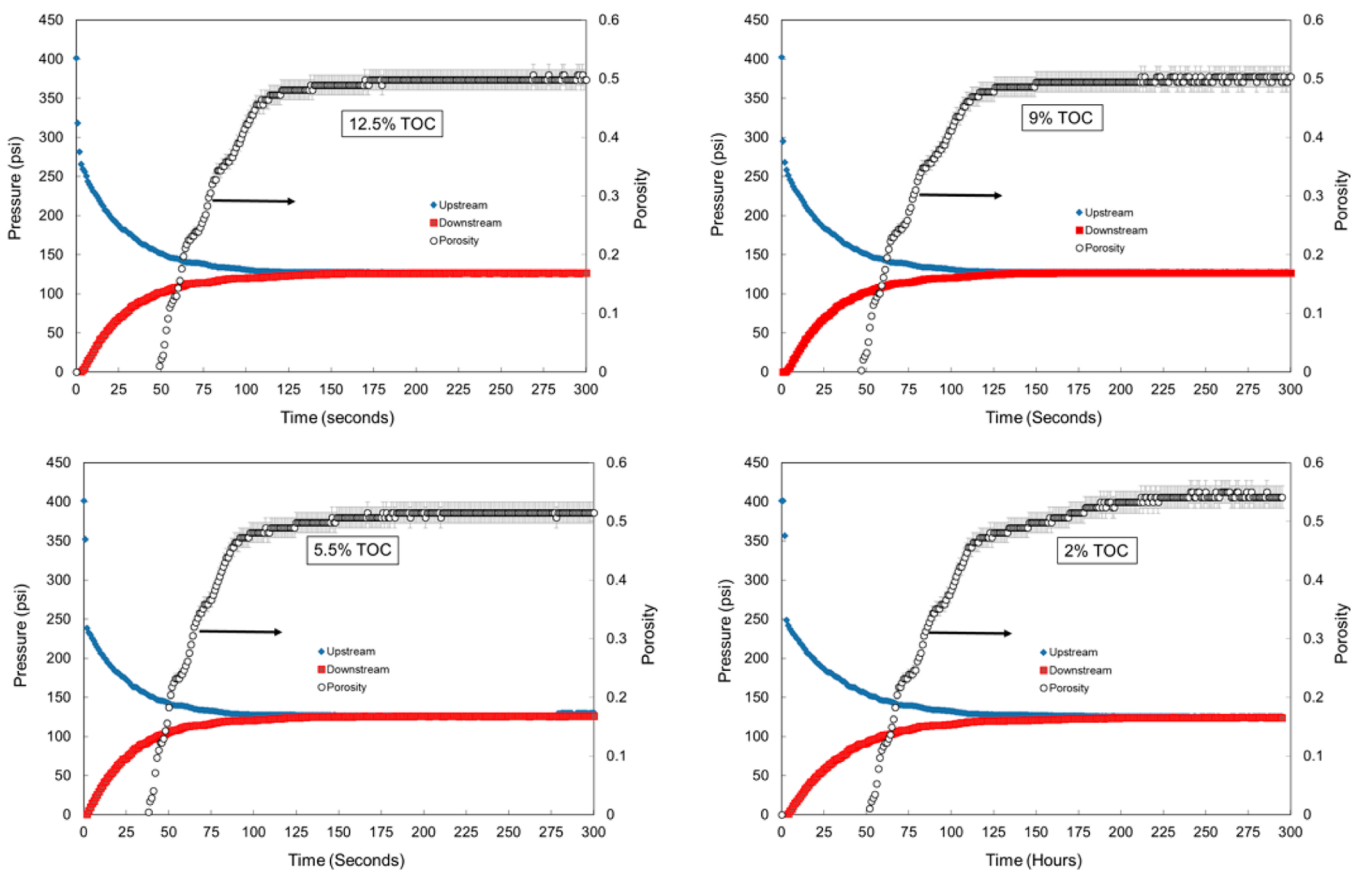
Figure 8. Effective porosity measurements on varying TOC samples.

The obtained porosities range from ~49% to 54% and are within 10% of each other. Although the powder was packed consistently for all samples at a constant volume, some variation may exist, because of differences in particle shape and size ratios.

Dynamic breakthrough measurements were then carried out at a temperature of 23.8 °C and under increasing pore pressure conditions. The system was initially flushed with helium at 50 sccm, to ensure no adsorbed gases on the adsorbate surface. At $t = 0$, CO_2 was introduced into the feed at a 50/50 concentration with helium. Figure 9 shows the resulting CO_2 breakthrough curves for each sample at increasing pore pressures. A delay in the breakthrough time is observed with increasing pressure and TOC. The delay in the breakthrough
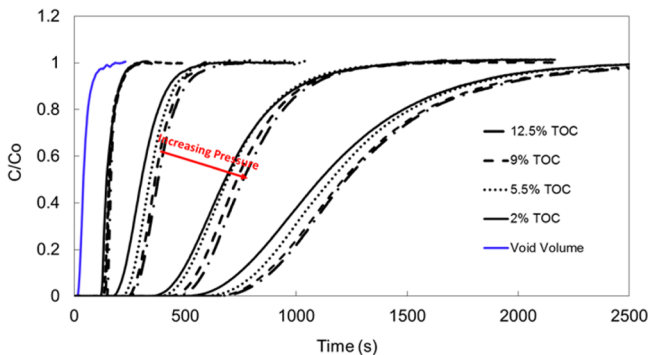

Figure 9. Comparison of normalized breakthrough curves on varying TOC content at a constant 50% CO_2 feed composition.

profile resulted in more moles of substance occupying the adsorbed phase.

The amount of CO_2 adsorbed is back-calculated by subtracting the free gas occupying the pore volume. The results are shown in Figure 10, where the CO_2 capacity is plotted as a function of total pressure equivalent to the sum of helium and CO_2 partial pressures, based on Dalton's Law. The samples illustrate the potential of carbon storage in shale formations where the CO_2 capacity significantly exceeds that of CH_4. Methane adsorption experiments carried out on different shale formations reveal a maximum monolayer capacity ranging from 50 SCF/ton to 80 SCF/ton.[52−54] The higher-order electric multipole moment (quadrupole moment) of the CO_2 molecule results in this strong adsorbent−adsorbate interaction, with shale acting as a natural sorbent material. The linear molecular geometry of CO_2, compared to a spherical CH_4 molecular geometry, also allows for better accessibility to the micropores. This, in fact, represents an important sequestration quality for CO_2 in shale formations. Experimental results also reveal a significant increase in CO_2 storage capacity with an increase in TOC content. A clear linear trend is obtained between TOC and CO_2 adsorption. Similar observations where an increase in methane capacity was noted with increasing TOC content on different samples from the black Devonian shales.[55−59]

Permeability results are shown in Figure 11, as a function of pore pressure. The permeability increases with pore pressure, because of an increase in the average kinetic energy of the gas molecules. Effects of slip flow are negligible at the powder scale, in these samples. Slip flow is typically evident in intact cores with very low porosities as pore channel diameters approach
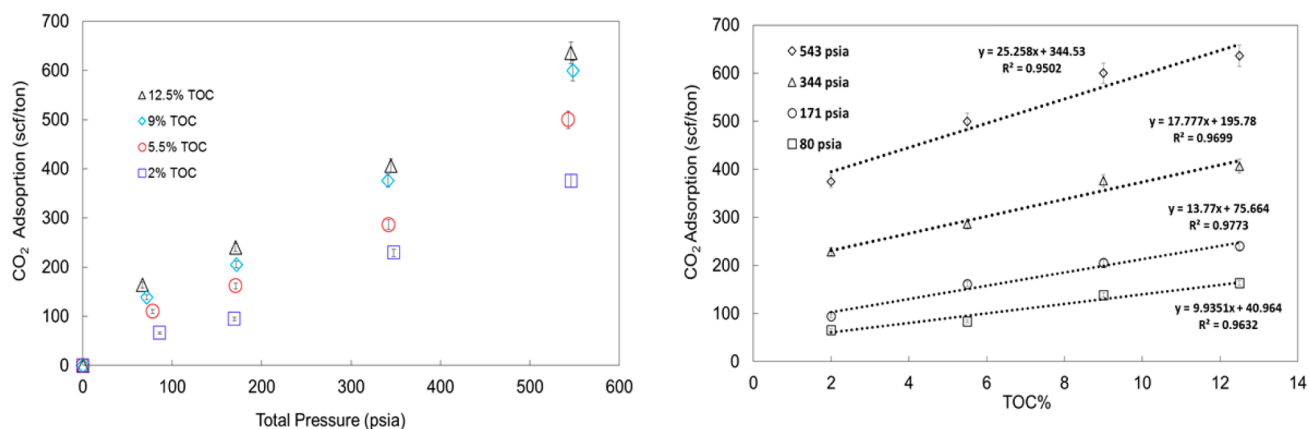
Figure 10. CO_2 adsorption capacity at 23.8 °C, as a function of pressure (left) and TOC% (right).
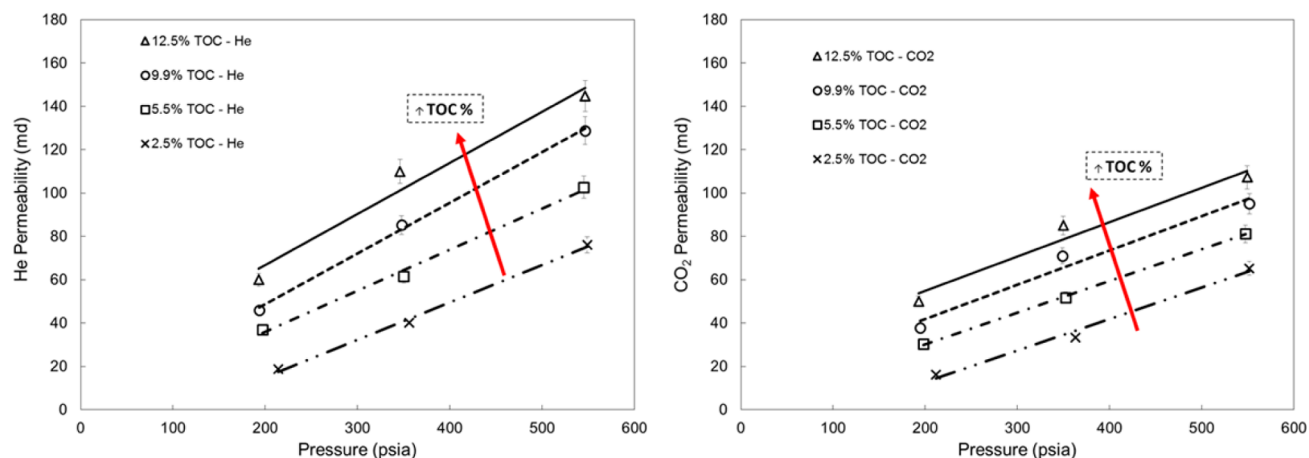

Figure 11. Helium (left) and CO_2 (right) permeability measurements on varying TOC% samples.

the mean free path of the gas. Results indicate an increase in helium permeability with increasing TOC. This is attributed to the complex internal structure of kerogen with significant nanometer-scale porosity that is ∼5 times greater than the nonorganic matrix, as documented by several authors through secondary electron imaging (SEI).[7,8,32,60] Because most of the pore volume resides in the kerogen, enhanced gas permeability is achieved with increasing TOC content.

Figure 11 also shows the impact of CO_2 on permeability where a reduction is observed due to swelling caused by adsorption. Volumetric swelling has been widely documented in coals with different gases such as CO_2, CH_4, and their mixtures.[4,61−66] Adsorption-induced swelling caused a reduction in permeability when measured with CO_2. CH_4 induces half as much swelling as CO_2 and, hence, the permeability reduction is not as severe. Other gases, such as H_2S, can swell even more than CO_2, resulting in a greater reduction in permeability.

4.1.2. Clay Analysis. Dynamic column breakthrough measurements were also carried out at increasing pore pressures using samples with varying illite content. Illite was chosen because it is the main clay mineral in shale formations.[67] In order to assess the impact of illite, in comparison to TOC, on adsorption, the experimental conditions were similar to the previous experiments carried out on the varying TOC samples. Porosity measurements on the packed bed were carried out on each sample. The porosities obtained range from ∼55% to 56%, as shown in Figure 12. Note that the upstream and downstream

pressure profiles equilibrated faster as the clay content increased.

Figure 13 shows the resulting breakthrough curves. A delay in the breakthrough time is noted with increasing pressure and illite fraction. By subtracting the dead and pore volume at each pressure, the CO_2 moles in the adsorbed phase were computed. The results are shown in Figure 14, where an increase in illite content led to an increase in adsorption capacity. This is attributed to the platy shape of clay minerals that allows for additional surface area for gas adsorption. Note that the 5% clay sample contains ∼94% quartz, whereas the 45% clay sample contains only 46% quartz. The increase in quartz concentration did not have an impact on CO_2 capacity, indicating negligible adsorption in quartz, as expected. It is clear that the illite content undermines the increase in quartz concentration. We can also observe from the isotherms, however, that increases in TOC resulted in greater adsorption capacity, compared to the increases in illite. A linear trend is still observed between the illite content and CO_2 adsorption. These results are in agreement with past studies on the adsorption behavior of different clay minerals including montmorillonite, illite, and kaolinite with different gases.[68−71] Results indicate a significant adsorption capacity for clay minerals in the following order: $SO_2 > CO_2 > CH_4 \geq N_2$. A positive relationship was also found between the CO_2 sorption and the micropore volume of clay minerals.

Permeability measurements were also carried out to determine the impact of increasing clay content on flow
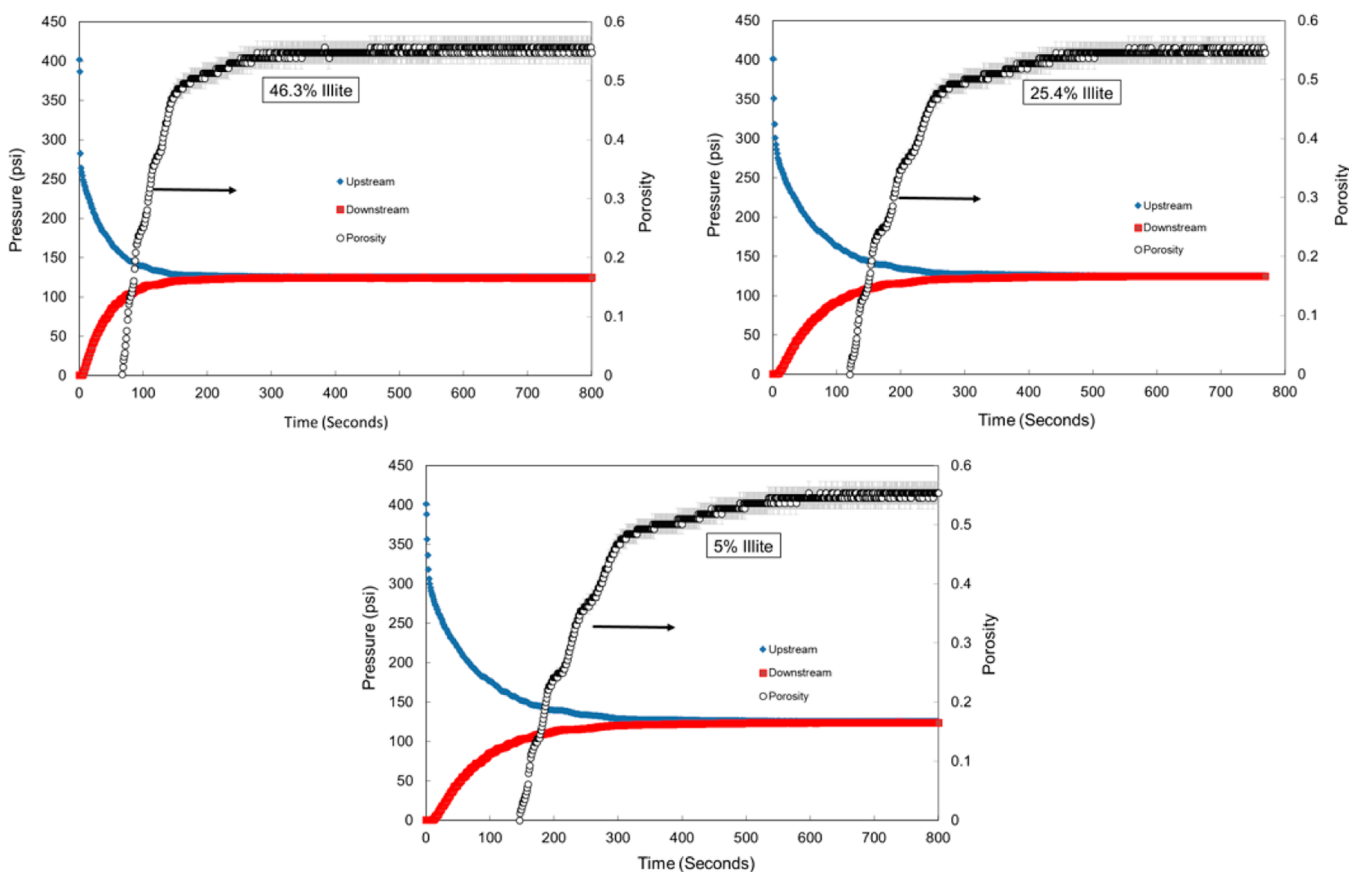
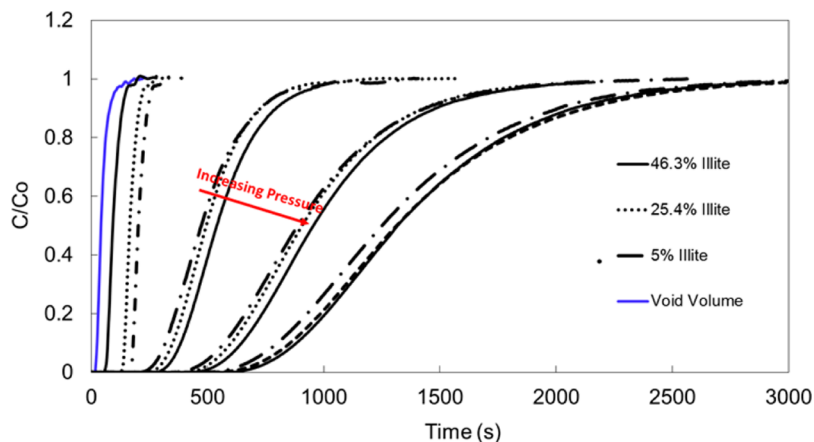Figure 12. Effective porosity measurements of varying illite content.

Figure 13. Comparison of normalized breakthrough curves on varying illite content, at a constant 50%CO_2 feed composition.

capacities. Permeability results are shown in Figure 15. Results indicate an enhanced permeability with increasing clay fraction and decreasing quartz fraction. Quartz is an extremely hard mineral; crystal systems of quartz include trigonal and hexagonal arrangements of silica tetrahedra that are resistive to fractures and microcracks. The nonporous nature of quartz contributes to its decreased gas permeability. Illites, however, are phyllosilicates that consist of mixed layers of Si tetrahedrons.[72] The interlayering characteristics of clay minerals results in large surface area/pore volume ratios, leading to a greater permeability.

Figure 16 shows the irreversible impact of CO_2 on permeability measured with helium after the last CO_2

adsorption point. Permeability reduction was 63% and 31.5% for the 46.3% and 25.4% illite series, respectively. The reduction is most significant on the 46.3% illite sample, indicating a proportionality between permeability reduction and the amount of CO_2 adsorbed. This decrease is attributed to clay swelling, which is common, because of the expansible nature of the separated clay sheets. The volumetric swelling strain with helium, CH_4, and CO_2 on pure illite and kaolinite has been investigated by several authors, including Heller and Zoback.[54] They concluded that the swelling strain was dependent on the increasing volume of gas adsorbed. We additionally note that the powdered samples may be overstating the role of clay swelling. Within intact shale samples, the
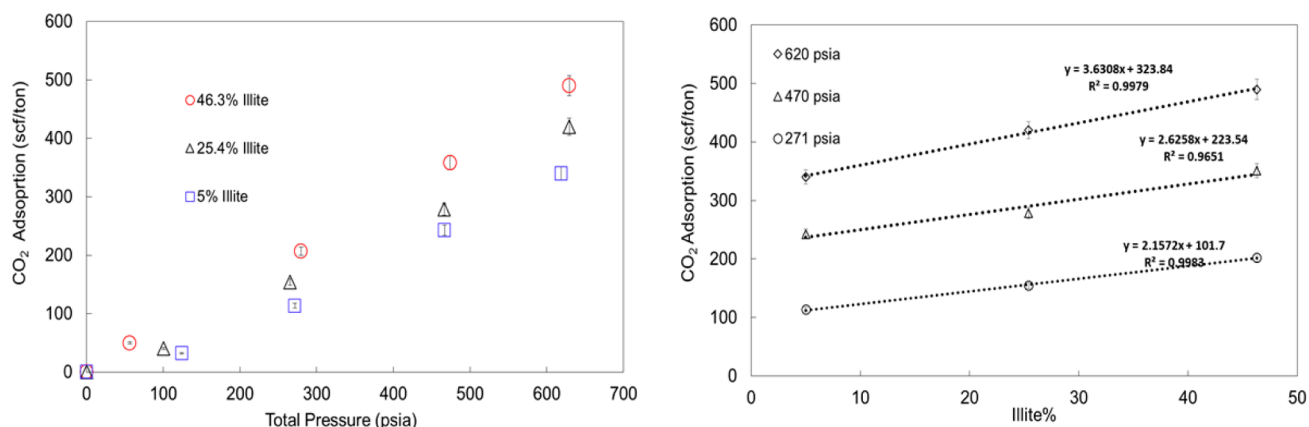
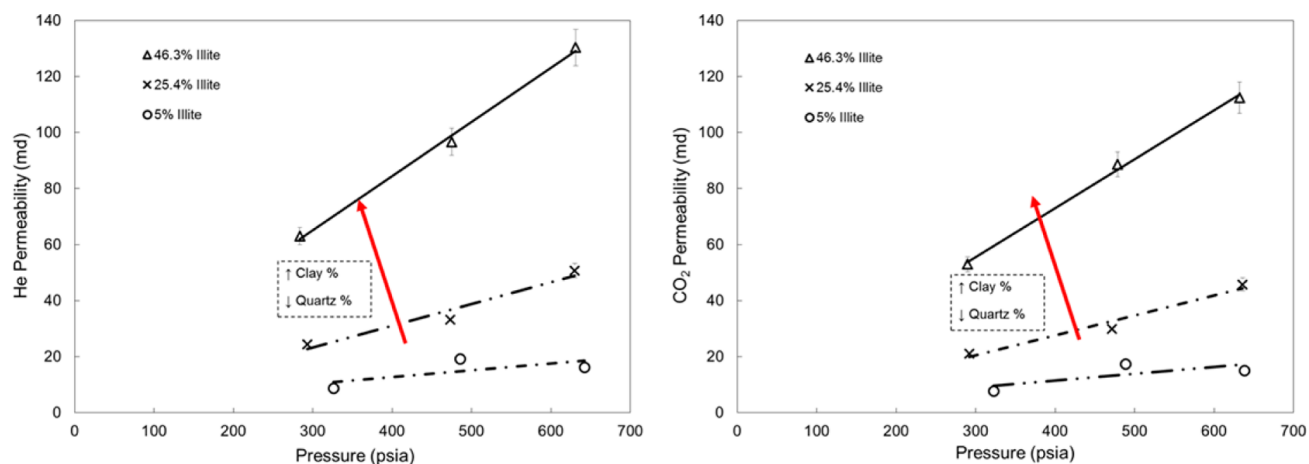**Figure 14.** CO_2 adsorption capacity at 23.8 °C, as a function of pressure (left) and illite content (right).

Figure 15. He (left) and CO_2 (right) permeability measurements on varying illite content samples.
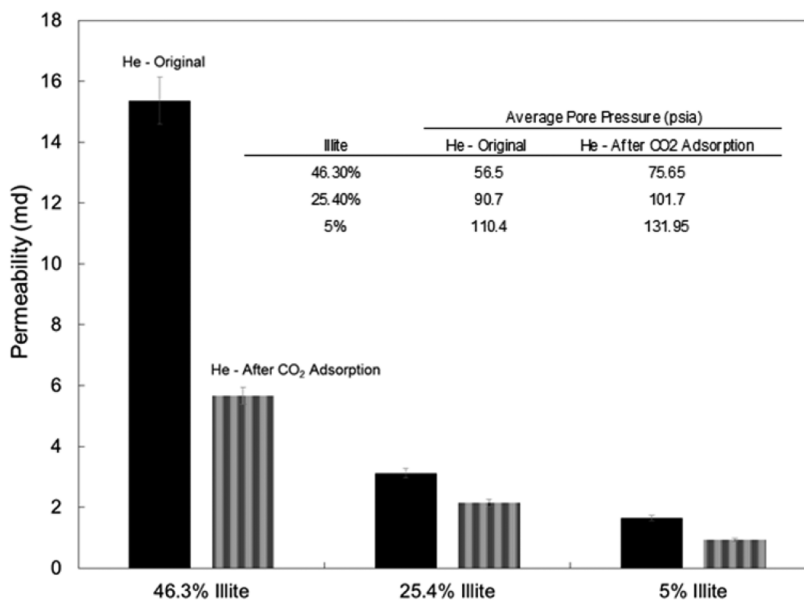

Figure 16. Helium permeability pre-CO_2 adsorption versus post-CO_2 adsorption.

organic matter is dispersed in the inorganic matrix and the organic deformation may be mitigated, in part, by the inorganic constituents.

4.2. Low-Pressure Adsorption Analysis. Results shown in Figure 17 are in agreement with the high-pressure dynamic breakthrough experiments. An increase in adsorption is noted with increasing TOC, as observed from the CO_2 and Ar isotherms in the top plots of Figure 17. Similarly, increasing the illite content also resulted in an increase in adsorption, as shown in the lower two plots of Figure 17. It is clear from the
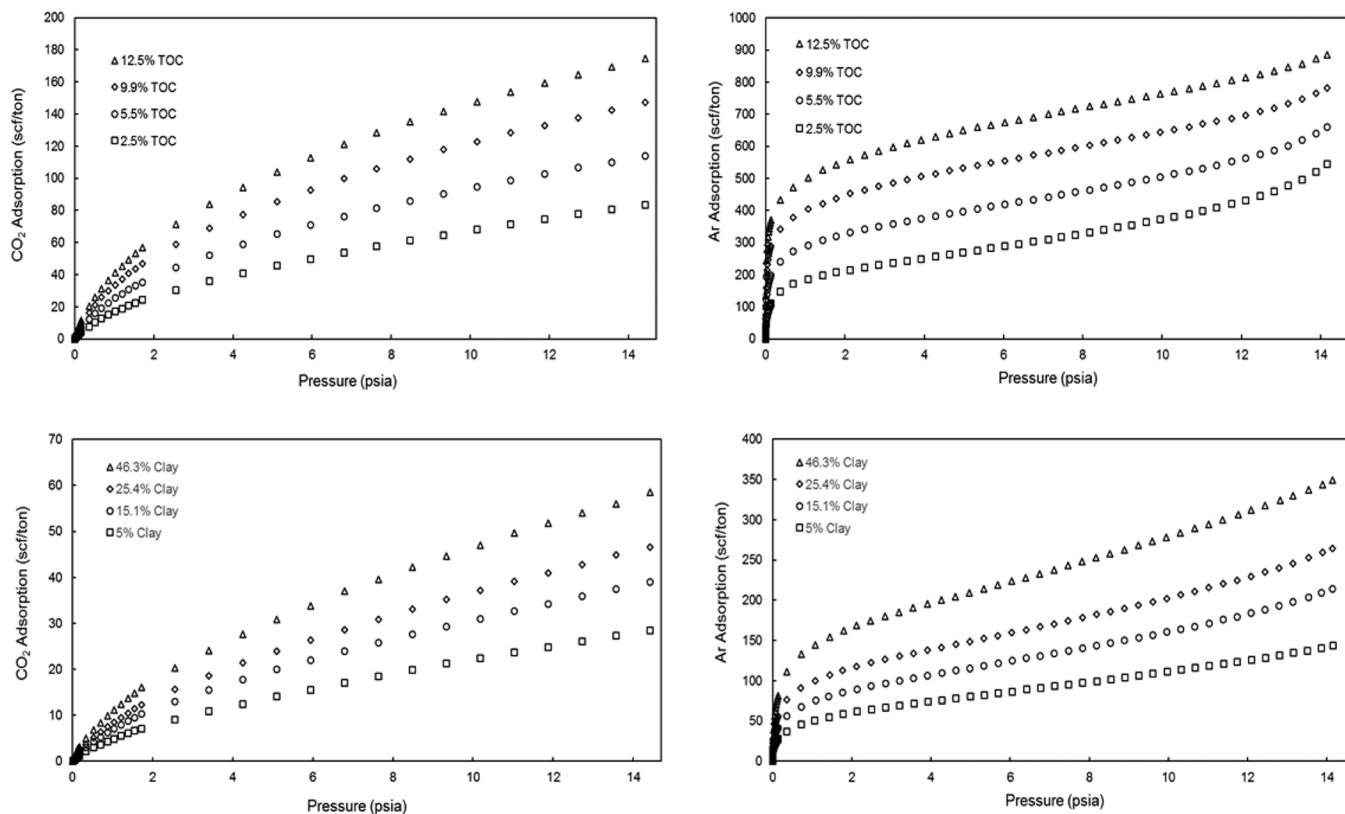
Figure 17. Low-pressure adsorption measurements using Ar at −186.15 °C and CO_2 at −0.15 °C. The TOC samples are the top two plots, and the illite series are the two lower plots.

Table 2. Ar and CO_2 Pore Volumes and Surface Area Results[a]

percent	CO₂ NLDFT on Carbon Slit Pore (0.3−1.47 nm)		Ar QSDFT on Carbon Cylindrical Pore (1.50−27.0 nm)		CO₂ + Ar (0.30−27.0 nm)	
	pore volume (cm^3/g)	surface area (m^2/g)	pore volume (cm^3/g)	surface area (m^2/g)	cumulative pore volume (cm^3/g)	cumulative surface area (m^2/g)
TOC Series						
2.0	0.008	25.7	0.019	19.8	0.027	45.5
5.5	0.011	34.7	0.021	25.9	0.032	60.6
9.0	0.014	45.3	0.023	31.6	0.037	76.9
12.5	0.017	53.5	0.024	32.7	0.041	86.1
Illite Series						
5.0	0.003	9.5	0.005	5.5	0.008	15.0
15.1	0.004	12.0	0.008	8.0	0.012	20.0
25.37	0.005	14.7	0.009	10.7	0.014	25.4
46.33	0.006	18.6	0.012	15.2	0.018	33.8

[a]Cumulative pore volumes are calculated by adding the CO_2 micropore results to the Ar results, adjusting for overlapping pore widths.

isotherms that weight percentage increases in TOC result in larger amounts of adsorption, compared to increases in the illite content, as evidenced by the change in y-axis scales in which the TOC series reaches 175 SCF/ton for CO_2 and 885 SCF/ton for Ar, whereas the illite series only reaches 58 SCF/ton for CO_2 and 348 SCF/ton for Ar. The adsorption capacity of Ar is greater than that of CO_2, because of the fact that both measurements were done at different temperatures. Because adsorption is an exothermic process,[73] temperature decreases result in rapid increases in adsorption in order to maintain system equilibrium based on Le Chatelier's principle.

In order to prevent double counting of the pore volumes and surface areas from pores with widths that overlap the CO_2 and Ar DFT models, if any pore volume or surface area was present

below 1.50 nm using Ar, then the Ar cumulative pore volumes and surface areas were adjusted by subtracting the amount measured below 1.50 nm from the Ar DFT cumulative pore volume at 27.0 nm. The cumulative pore volumes and surface areas of the samples were calculated by adding the CO_2 measurements (pores 0.3−1.475 nm in size) to the Ar measurements (~1.50−27.04 nm). While there is a small gap in the pore diameters between 1.475 nm and 1.50 nm, it can be assumed to be a negligible amount of pore volume and surface area. The CO_2 and adjusted Ar measurement results were added together to determine the CO_2 + Ar and cumulative pore volume and surface areas, as shown in Table 2.

The average pore width decreased with increasing TOC, because of the presence of micropores and fine mesopores in
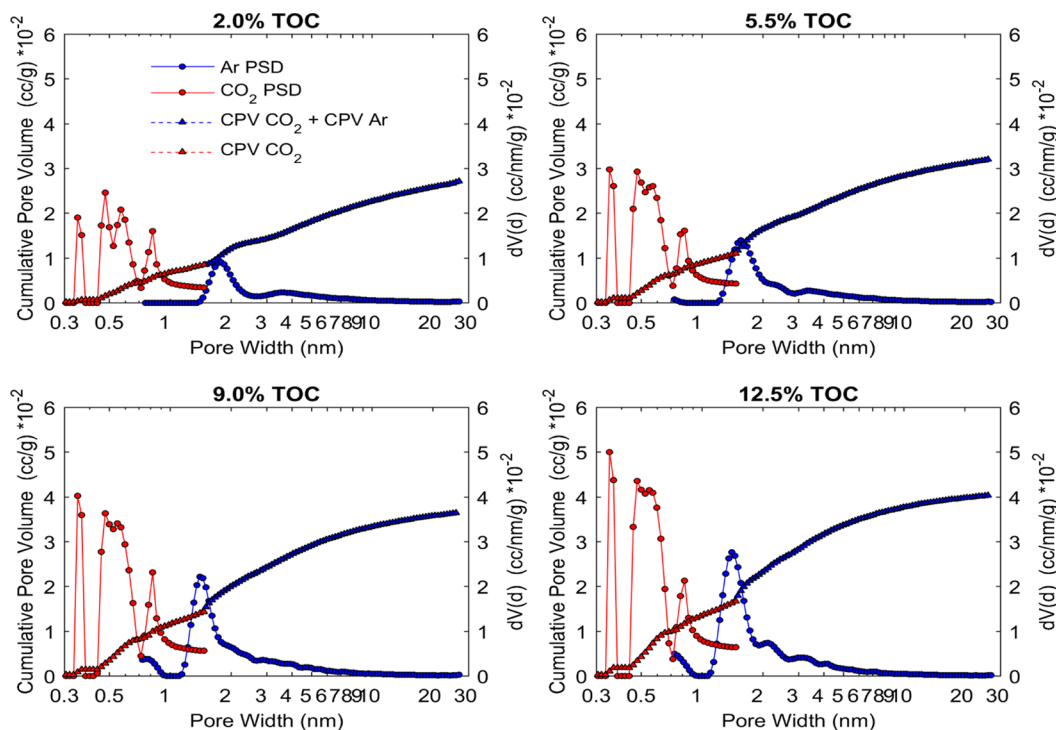
Figure 18. Pore-size distribution with CO_2 and Ar on varying TOC samples. The cumulative pore volume increases with each increase in TOC.
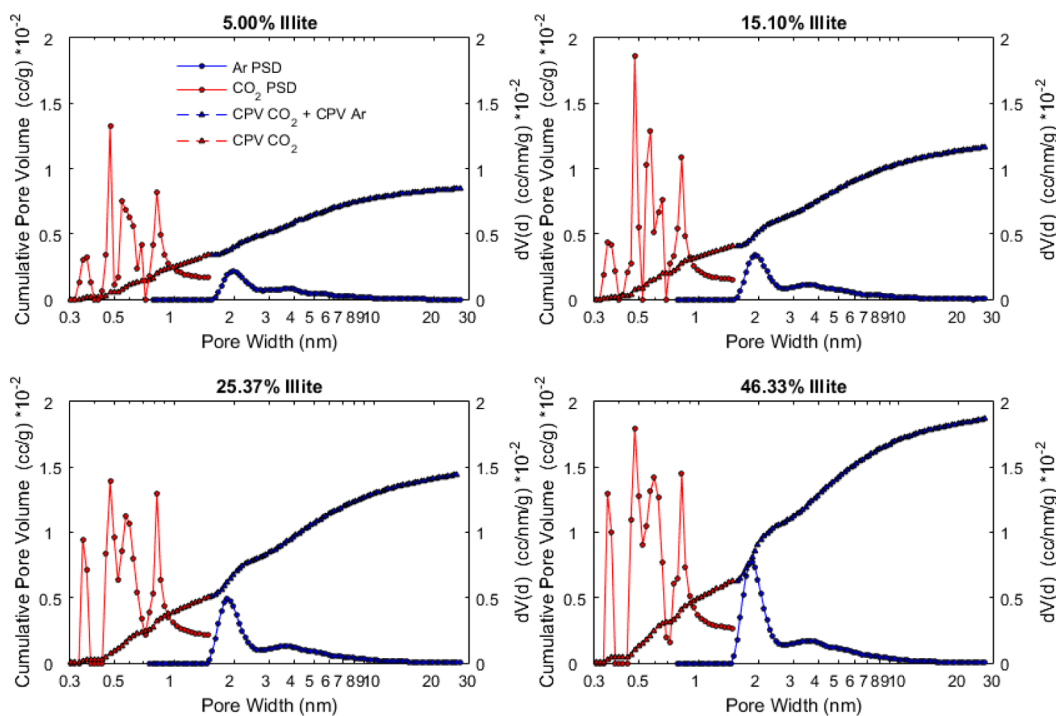

Figure 19. Pore-size distribution with CO_2 and Ar on samples with increasing amounts of illite.

the kerogen. This is consistent with the literature, which shows that carbon content such as kerogen plays a primary role in the pore volume of shales, with clays such as illite having a secondary role.[56,58,59]

Pore-size distribution results indicate an increase in surface area with increasing TOC in the micropores and in the fine mesopores (from 2 nm to 10 nm), as shown in Figure 18. Increases in illite content also showed an increase in surface area in the same pore size regions, as shown in Figure 19. It is

clear that each weight percent increase in TOC has a larger influence on the pore volume and surface area than does each weight percentage increase in illite content. Note that an ~3.5 wt % increase in TOC results in an ~0.005 cm^3/g increase in surface area, whereas it takes a ~20 wt % increase in the illite to achieve a 0.003 cm^3/g increase. The TOC series pore volume increases by ~1.4 × 10^{-3} cm^3/g for each weight percent increase in TOC, whereas the illite series pore volume only increases by ~0.4 × 10^{-3} cm^3/g for each weight percent

increase in illite. These trends are reflected in Figure 18, which shows the increases in the adjusted combined CO_2 + Ar cumulative pore volume. This increase in pore volume for every 3.5 wt % increase in TOC is reflected in both CO_2- and Ar-accessible micropores and fine mesopores. This shows that, for each weight percent increase in either TOC or illite, the pore volume increase in the TOC series is ~3.5 times that of the illite series.

CONCLUSION

An experimental apparatus was custom built to conduct dynamic breakthrough adsorption measurements for the first time on shales. Unlike conventional static adsorption measurement techniques, the dynamic method is capable of describing gas adsorption through the measurement of the adsorbent concentration profile with time. The pressure differential developed at the two ends of the rock column made the experimental setup capable of measuring the permeability of the sample using Darcy's law. To assess the impact of shale mineralogy on gas flow and storage potential, experiments were carried out on powdered idealized shale samples with defined TOC and illite contents. Results show an increase in permeability and CO_2 adsorption with either increasing TOC or illite content. Permeability reduction was also noted with CO_2 due to adsorption-induced swelling. Given the large surface area and pore volume in the kerogen, increases in TOC content proved to be most significant to adsorption, compared to increases in other shale constituents. The CO_2 adsorption capacity increased by ~19.5 scf/ton for each weight percent increase in TOC, compared to an average increase of 3.33 scf/ton for each weight percent increase in illite, as shown in Figure 20.
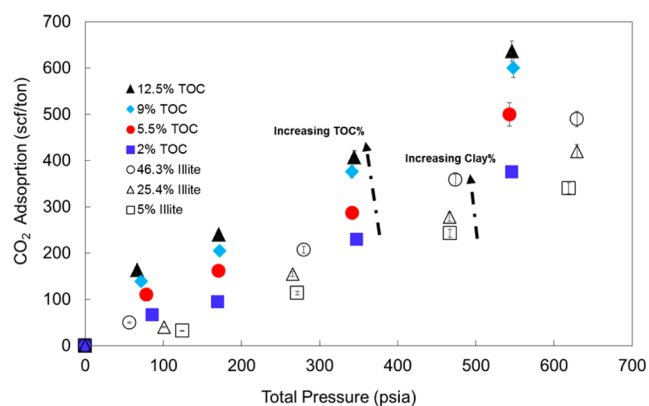

Figure 20. Summary of TOC% and illite% impact on adsorption at 23.8 °C.

The storage and flow capacity results were consistent with the findings from the low-pressure adsorption measurements carried out using an Autosorb iQ_2 instrument (Quantachrome Instruments). Pore-size distribution results indicated an increase in surface area and pore capacity with either increasing TOC or illite content, which allowed additional space for CO_2 adsorption. These experimental results shed light on the magnitude of CO_2 adsorption and its effect on transport mechanisms in shale formations. Significant CO_2 adsorption capacities illustrate the potential for carbon storage, as well as its promising application for enhanced gas recovery mechanisms. The conclusions support previous studies by Wang et al.[25] and Middleton et al.,[26] which proposed the use of supercritical CO_2 as a fracturing fluid to reduce its carbon footprint, in addition to enhancing methane production. The use of CO_2 also eliminates the need for large volumes of water for hydraulic fracturing as well as the long time required to flow back, treat, and dispose of water.

AUTHOR INFORMATION

Corresponding Author
*Postal Address: Department of Energy Resources Engineering, Stanford University, 367 Panama Street, Green Earth Sciences 074, Stanford, CA 94305-2220, USA. Tel.: 650-723-1218. Fax: 650-725-2099. E-mail: kovscek@stanford.edu.

ORCID
Randall Holmes: 0000-0002-5047-5528
Anthony R. Kovscek: 0000-0003-1336-384X

Notes
The authors declare no competing financial interest.

REFERENCES

(1) Alnoaimi, K. R. *Influence of Cracks and Microcracks on Flow and Storage Capacities of Gas Shales at Core-level*, Thesis, Stanford University: Stanford, CA, 2016.
(2) Kovscek, A. R.; Cakici, M. D. Geologic storage of carbon dioxide and enhanced oil recovery. Cooptimization of storage and recovery. *Energy Convers. Manage.* **2005**, *46* (11−12), 1941−1956.
(3) Firouzi, M.; Rupp, E. C.; Liu, C. W.; Wilcox, J. Molecular simulation and experimental characterization of the nanoporous structures of coal and gas shale. *Int. J. Coal Geol.* **2014**, *121*, 123−128.
(4) Vishal, V.; Singh, L.; Pradhan, S. P.; Singh, T. N.; Ranjith, P. G. Numerical modeling of Gondwana coal seams in India as coalbed methane reservoirs substituted for carbon dioxide sequestration. *Energy* **2013**, *49*, 384−394.
(5) Vishal, V.; Singh, T. N.; Ranjith, P. G. Influence of sorption time in CO_2-ECBM process in Indian coals using coupled numerical simulation. *Fuel* **2015**, *139*, 51−58.
(6) Clarkson, C. R.; Solano, N.; Bustin, R. M.; Bustin, A. M. M.; Chalmers, G. R. L.; He, L.; Melnichenko, Y. B.; Radliński, A. P.; Blach, T. P. Pore structure characterization of North American shale gas reservoirs using USANS/SANS, gas adsorption, and mercury intrusion. *Fuel* **2013**, *103*, 606−616.
(7) Wang, F. P.; Reed, R. M. Pore networks and fluid flow in gas shales. In *SPE Annual Technical Conference and Exhibition*. Society of Petroleum Engineers, New Orleans, Louisiana, USA, 4−7 October, 2009.
(8) Bustin, R. M.; Bustin, A. M. M.; Cui, A.; Ross, D.; Pathi, V. M. Impact of Shale Properties on Pore Structure and Storage Characteristics. Presented at the *SPE Shale Gas Production Conference*, Fort Worth, TX, Nov. 16, 2008; Paper No. SPE-119892-MS10.2118/119892-MS.
(9) Javadpour, F. Nano pores and apparent permeability of gas flow in mud rocks (shales and siltstone). *J. Can. Pet. Technol.* **2009**, *48*, 16−21.
(10) Freeman, C. M.; Moridis, G. J.; Blasingame, T. A. A numerical study of microscale flow behavior in tight gas and shale gas reservoir systems. *Transp. Porous Media* **2011**, *90*, 253−268.

(11) Gasparik, M.; Bertier, P.; Gensterblum, Y.; Ghanizadeh, A.; Krooss, B. M.; Littke, R. Geological controls on the methane storage capacity in organic-rich shales. *Int. J. Coal Geol.* **2014**, *123*, 34−51.

(12) Ji, L. M.; Zhang, T. W.; Milliken, K. L.; Qu, J. L.; Zhang, X. L. Experimental investigation of main controls to methane adsorption in clay-rich rocks. *Appl. Geochem.* **2012**, *27* (12), 2533−2545.

(13) Ross, D. J. K.; Bustin, R. M. Impact of mass balance calculations on adsorption capacities in microporous shale gas reservoirs. *Fuel* **2007**, *86* (17−18), 2696−2706.

(14) Valenza, J. J.; Drenzek, N.; Marques, F.; Pagels, M.; Mastalerz, M. Geochemical controls on shale microstructure. *Geology* **2013**, *41* (5), 611−614.

(15) Chalmers, G. R.; Bustin, R. M.; Power, I. M. Characterization of gas shale pore systems by porosimetry, pycnometry, surface area, and field emission scanning electron microscopy/transmission electron microscopy image analyses, Examples from the Barnett, Woodford, Haynesville, Marcellus, and Doig units. *AAPG Bull.* **2012**, *96* (6), 1099−1119.

(16) Liu, Y.; Wilcox, J. CO_2 Adsorption on Carbon Models of Organic Constituents of Gas Shale and Coal. *Environ. Sci. Technol.* **2011**, *45* (2), 809−814.

(17) Liu, Y.; Wilcox, J. Molecular Simulation Studies of CO_2 Adsorption by Carbon Model Compounds for Carbon Capture and Sequestration Applications. *Environ. Sci. Technol.* **2013**, *47* (1), 95−101.

(18) Loucks, R. G.; Reed, R. M.; Ruppel, S. C.; Jarvie, D. M. Morphology, genesis, and distribution of nanometer-scale pores in siliceous mudstones of the Mississippian Barnett shale. *J. Sediment. Res.* **2009**, *79* (12), 848−861.

(19) Schnoor, J. L. Shale Gas and Hydrofracturing. *Environ. Sci. Technol.* **2012**, *46* (9), 4686−4686.

(20) Waters, G. A.; Dean, B. K.; Downie, R. C.; Kerrihard, K. J.; Austbo, L.; McPherson, B. Simultaneous Hydraulic Fracturing of Adjacent Horizontal Wells in the Woodford Shale. Presented at the *SPE Hydraulic Fracturing Technology Conference*, The Woodlands, TX, Jan. 19, 2009; Paper No. 11963510.2118/119635-MS.

(21) Chen, D.; Pan, Z. J.; Ye, Z. H. Dependence of gas shale fracture permeability on effective stress and reservoir pressure, Model match and insights. *Fuel* **2015**, *139*, 383−392.

(22) Sakhaee-Pour, A.; Bryant, S. L. Pore structure of shale. *Fuel* **2015**, *143*, 467−475.

(23) Jessen, K.; Tang, G.-Q.; Kovscek, A. R. Laboratory and Simulation Investigation of Enhanced Coalbed Methane Recovery by Gas Injection. *Transp. Porous Media* **2008**, *73* (2), 141−159.

(24) Kang, S. M.; Fathi, E.; Ambrose, R. J.; Akkutlu, I. Y.; Sigal, R. F. Carbon dioxide storage capacity of organic-rich shales. Presented at the *SPE Annual Technical Conference and Exhibition*, Florence, Italy, Sept. 19, 2010; Paper No. 13458310.2118/134583-MS.

(25) Wang, H.; Li, G.; Shen, Z. A feasibility analysis on shale gas exploitation with supercritical carbon dioxide. *Energy Sources, Part A* **2012**, *34* (15), 1426−1435.

(26) Middleton, R. S.; Carey, J. W.; Currier, R. P.; Hyman, J. D.; Kang, Q.; Karra, S.; Jiménez-Martínez, J.; Porter, M. L.; Viswanathan, H. S. Shale gas and non-aqueous fracturing fluids: Opportunities and challenges for supercritical CO_2. *Appl. Energy* **2015**, *147*, 500−509.

(27) Fathi, E.; Akkutlu, I. Y. Multi-component gas transport and adsorption effects during CO_2 injection and enhanced shale gas recovery. *Int. J. Coal Geol.* **2014**, *123*, 52−61.

(28) Sigal, R. F. Mercury Capillary Pressure Measurements on Barnett Core. SPE. *Reservoir Eval. Eng.* **2013**, *16* (4), 432−442.

(29) Curtis, M. E.; Sondergeld, C. H.; Ambrose, R. J.; Rai, C. S. Microstructural investigation of gas shales in two and three dimensions using nanometer-scale resolution imaging. *AAPG Bull.* **2012**, *96* (4), 665−677.

(30) Dewers, T. A.; Heath, J.; Ewy, R.; Duranti, L. Three-dimensional pore networks and transport properties of a shale gas formation determined from focused ion beam serial imaging. *Int. J. Oil, Gas Coal Technol.* **2012**, *5* (2−3), 229−248.

(31) Sarker, R.; Batzle, M. Anisotropic elastic moduli of the Mancos B shale-An experimental study. Presented at the *2010 SEG Annual Meeting*, Denver, Colorado, 17−22 October, 2010.

(32) Sondergeld, C. H.; Ambrose, R. J.; Rai, C. S.; Moncrieff, J. Micro-structural studies of gas shales. Presented at the *SPE Unconventional Gas Conference*; Society of Petroleum Engineers, Pittsburgh, Pennsylvania, USA, 23−25 February, 2010.

(33) Akin, S.; Kovscek, A. R. Computed tomography in petroleum engineering research. *Geol. Soc. Spec. Publ.* **2003**, *215* (1), 23−38.

(34) Vega, B.; Dutta, A.; Kovscek, A. R. CT imaging of low-permeability, dual-porosity systems using high X-ray contrast gas. *Transp. Porous Media* **2014**, *101* (1), 81−97.

(35) Clarkson, C. R., Wood, J. M., Aquino, S. D., Freeman, M., Birss, V. Nanopore Structure Analysis and Permeability Predictions for a Tight Gas/Shale Reservoir Using Low-Pressure Adsorption and Mercury Intrusion Techniques. Paper presented at the *Americas Unconventional Resources Conference*, Pittsburgh, PA, USA, 2012.

(36) Kuila, U.; Prasad, M. Specific surface area and pore-size distribution in clays and shales. *Geophys. Prospect.* **2013**, *61* (2), 341−362.

(37) Labani, M. M.; Rezaee, R.; Saeedi, A.; Hinai, A. A. Evaluation of pore size spectrum of gas shale reservoirs using low pressure nitrogen adsorption, gas expansion and mercury porosimetry: A case study from the Perth and Canning Basins, Western Australia. *J. Pet. Sci. Eng.* **2013**, *112*, 7−16.

(38) Rajendran, A.; Kariwala, V.; Farooq, S. Correction procedures for extra-column effects in dynamic column breakthrough experiments. *Chem. Eng. Sci.* **2008**, *63* (10), 2696−2706.

(39) Hofman, P. S.; Rufford, T. E.; Chan, K. I.; May, E. F. A dynamic column breakthrough apparatus for adsorption capacity measurements with quantitative uncertainties. *Adsorption* **2012**, *18* (3−4), 251−263.

(40) Park, I.; Knaebel, K. S. Adsorption breakthrough behavior: Unusual effects and possible causes. *AIChE J.* **1992**, *38* (5), 660−670.

(41) Han, R.; Wang, Y.; Zhao, X.; Wang, Y.; Xie, F.; Cheng, J.; Tang, M. Adsorption of methylene blue by phoenix tree leaf powder in a fixed-bed column, experiments and prediction of breakthrough curves. *Desalination* **2009**, *245* (1), 284−297.

(42) Asadi, T.; Ehsani, M. An Experimental Study of Adsorption Breakthrough Curves for CO_2/CH_4 Separation in a Fixed Bed of Nanoporous Shaped Copper Trimesate Metal Organic Framework. *Iranian J. Oil Gas Sci. Technol.* **2013**, *2* (4), 54−66.

(43) He, J.; To, J.; Mei, J.; Bao, Z.; Wilcox, J. Facile Synthesis of Nitrogen-doped Porous Carbon for Selective CO2 Capture. *Energy Procedia* **2014**, *63*, 2144−2151.

(44) Bao, Z.; To, J.; He, J.; Wilcox, J.; Mei, J. Microporous/Mesoporous Carbon. U.S. Patent Application 14/701,322, 2015.

(45) Sircar, S. Recent developments in macroscopic measurement of multicomponent gas adsorption equilibria, kinetics, and heats. *Ind. Eng. Chem. Res.* **2007**, *46* (10), 2917−2927.

(46) Agrawal, A.; Wei, Y.; Holditch, S. A technical and economic study of completion techniques in five emerging US gas shales: A Woodford shale example. *SPE Drill. Completion* **2012**, *27*, 39−49.

(47) Kohli, A.; Zoback, M. Frictional properties of shale reservoir rocks. *J. Geophys. Res. Solid Earth* **2013**, *118*, 5109−5125.

(48) Al Ismail, M. *Influence of Nanopores on the Transport of Gas and Gas-Condensate in Unconventional Resources.* Ph.D. Dissertation, Stanford University, Stanford, CA, 2016.

(49) Materials Data, I *Jade XRD Pattern Processing Version 6.5*, 2002.

(50) Scheidegger, A. E. *The Physics of Flow through Porous Media*, 3rd Edition; University of Toronto Press: Toronto, Canada, 1974.

(51) Reichenberg, D. *Fluids and Fluids Mixtures. Symposium Transport Properties*; National Engineering Laboratory: East Kilbride, Glasgow, Scotland, May 1979.

(52) Aljamaan, H., Alnoaimi, K., Kovscek, A. In-depth experimental investigation of shale physical and transport properties. *Unconventional Resources Technology Conference (URTEC)* **2013**, (August) 1120−112910.1190/urtec2013-114

(53) Alnoaimi, K. R.; Kovscek, A. R. Experimental and numerical analysis of gas transport in shale including the role of sorption. In *SPE*

Annual Technical Conference and Exhibition. Society of Petroleum Engineers, September 2013.

(54) Heller, R.; Zoback, M. Adsorption of methane and carbon dioxide on gas shale and pure mineral samples. *J. Unconv. Oil Gas Resour.* **2014**, *8*, 14−24.

(55) Chalmers, G. R.; Bustin, R. M. Lower Cretaceous gas shales in northeastern British Columbia, Part I: geological controls on methane sorption capacity. *Bull. Can. Pet. Geol.* **2008**, *56* (1), 1−21.

(56) Lu, X.; Li, F.; Watson, A. Adsorption measurements in Devonian shales. *Fuel* **1995**, *74* (4), 599−603.

(57) Nuttall, B.; Eble, C.; Drahovzal, J.; Bustin, R. *Analysis of Devonian black shales in Kentucky for potential carbon dioxide sequestration and enhanced natural gas production.* Kentucky Geologic Survey/University of Kentucky: Lexington, KY, 2005.

(58) Ross, D. J.; Bustin, R. The importance of shale composition and pore structure upon gas storage potential of shale gas reservoirs. *Mar. Pet. Geol.* **2009**, *26*, 916−927.

(59) Zhang, T.; Ellis, G. S.; Ruppel, S. C.; Milliken, K.; Yang, R. Effect of organic-matter type and thermal maturity on methane adsorption in shale-gas systems. *Org. Geochem.* **2012**, *47*, 120−131.

(60) Curtis, M. E., Ambrose, R. J., Sondergeld, C. H. Structural characterization of gas shales on the micro-and nano-scales. Presented at the *Canadian Unconventional Resources and International Petroleum Conference*; Society of Petroleum Engineers, Calgary, Alberta, Canada, 19−21 October, 2010.

(61) Rodrigues, C. F.; Lemos De Sousa, M. J. The measurement of coal porosity with different gases. *Int. J. Coal Geol.* **2002**, *48* (3), 245−251.

(62) Pini, R., Ottiger, S., Burlini, L., Storti, G., Mazzotti, M. Role of adsorption and swelling on the dynamics of gas injection in coal. *J. Geophys. Res.* **2009**, *114* (B4), B0420310.1029/2008JB005961

(63) Pan, Z.; Connell, L. D.; Camilleri, M. Laboratory characterization of coal reservoir permeability for primary and enhanced coalbed methane recovery. *Int. J. Coal Geol.* **2010**, *82*, 252−261.

(64) Day, S.; Fry, R.; Sakurovs, R. Swelling of coal in carbon dioxide, methane and their mixtures. *Int. J. Coal Geol.* **2012**, *93*, 40−48.

(65) Adeboye, O. O.; Bustin, R. M. Variation of gas flow properties in coal with probe gas, composition and fabric: Examples from western Canadian sedimentary basin. *Int. J. Coal Geol.* **2013**, *108*, 47−52.

(66) Durucan, S.; Ahsanb, M.; Shia, J.-Q. Matrix shrinkage and swelling characteristics of European coals. *Energy Procedia* **2009**, *1*, 3055−3062.

(67) Yaalon, D. H. Mineral composition of average shale. *Clay Miner.* **1962**, *5* (27), 31−36.

(68) Busch, A.; Alles, S.; Gensterblum, Y.; Prinz, D.; Dewhurst, D. N.; Raven, M. D.; Stanjek, H.; Krooss, B. M. Carbon dioxide storage potential of shales. *Int. J. Greenhouse Gas Control* **2008**, *2*, 297−308.

(69) Chiou, C. T.; Rutherford, D. W.; Manes, M. Sorption of N1 and EGME vapors on some soils, clays, and mineral oxides and determination of sample surface areas by use of sorption data. *Environ. Sci. Technol.* **1993**, *27*, 1587−1594.

(70) Melnitchenko, A.; Thompson, J. G.; Volzone, C.; Ortiga, J. Selective gas adsorption by metal exchanged amorphous kaolinite derivatives. *Appl. Clay Sci.* **2000**, *17*, 35−53.

(71) Venaruzzo, J. L.; Volzone, C.; Rueda, M. L.; Ortiga, J. Modified bentonitic clay minerals as adsorbents of CO, CO_2 and SO_2 gases. *Microporous Mesoporous Mater.* **2002**, *56* (1), 73−80.

(72) Srodon, J.; Elsass, F.; McHardy, W. J.; Morgan, D. J. Chemistry of Illite-smectite inferred from TEM measurements of fundamental particles. *Clay Miner.* **1992**, *27*, 137−158.

(73) Myers, A. L.; Monson, P. A. Physical adsorption of gases: the case for absolute adsorption as the basis for thermodynamic analysis. *Adsorption* **2014**, *20* (4), 591−622.